

First results of a site-testing programme at Mount Shatdzhatmaz during 2007–2009

V. Kornilov,^{*} N. Shatsky, O. Voziakova, B. Safonov, S. Potanin and M. Kornilov

Sternberg Astronomical Institute, Universitetsky prosp. 13, 119992 Moscow, Russia

Accepted 2010 June 14. Received 2010 June 14; in original form 2010 May 26

ABSTRACT

We present the first results of site testing performed at Mt Shatdzhatmaz in the Northern Caucasus, where the new Sternberg Astronomical Institute 2.5-m telescope will be installed. An automatic site-monitor instrumentation and functionality are described, together with the methods of measurement of the basic astroclimate and weather parameters. The clear night-sky time derived on the basis of 2006–2009 data amounts to 1340 h per year.

Principal attention is given to measurement of the optical-turbulence altitude distribution, which is the most important characteristic affecting the performance of optical telescopes. For the period from 2007 November–2009 October, more than 85 000 turbulence profiles were collected using the combined Multi Aperture Scintillation Sensor and Differential Image Motion Monitor (MASS/DIMM) instrument. The statistical properties of the turbulent atmosphere above the summit are derived and the median values for seeing $\beta_0 = 0.93$ arcsec and free-atmosphere seeing $\beta_{\text{free}} = 0.51$ arcsec are determined. Together with the estimations of isoplanatic angle $\theta_0 = 2.07$ arcsec and time constant $\tau_0 = 2.58$ ms, these are the first representative results obtained for Russian sites, and are necessary for the development of modern astronomical observation techniques like adaptive optics.

Key words: atmospheric effects – site testing – techniques: miscellaneous.

1 INTRODUCTION

Nearly twenty years have passed since astronomers recognized that progress in ground-based optical observations depends fully on success in minimizing the destructive influence of the atmosphere. Indeed, the new-generation telescopes have reached maximal technology-limited sizes and diffraction-limited optical quality and the detectors used have attained nearly 100 per cent quantum efficiency. The telescope performance is determined then by the last parameter in the Bowen (1964) formula: the seeing.

The capabilities of a large telescope may be significantly boosted by the use of adaptive optical systems (AO). Meanwhile, knowledge of seeing statistics alone is insufficient for assessment of the AO perspectives at a given site. The design of AO (see Vernin et al. 1991; Roddier 1999; Tokovinin, Baumont & Vasquez 2003a; Wilson et al. 2003; Fuensalida et al. 2004) demands information on the altitude distribution of *optical turbulence* (OT). About 15 yr ago this requirement intensified site-testing studies, aimed at collecting reliable and statistically significant data on OT both for prospective sites (Vernin, Muñoz-Tuñón & Sarazin 2008; Saunders et al. 2009; Schoeck et al. 2009) and at existing observatories (Tokovinin et al. 2003a; Thomsen, Britton & Pickles 2007; Wilson, Butterley & Sarazin 2009).

The site selection for the new 2.5-m telescope of Sternberg Astronomical Institute (SAI, Moscow University) has revealed the absence of reliable and contemporary information on the astroclimate of the Caucasian region of Russia. For this reason, the Shatdzhatmaz summit site near Kislovodsk city was chosen on the basis of sparse results obtained 40–50 yr ago and secondary factors.

The night-time astroclimatic characteristics of this place were measured at the end of the 1950s with a star-trails photographic technique (Darchiya, Schmeel & Darchiya 1960; Boshnjakovitch et al. 1962), which was standard for that time. Authors demonstrated the site's advantages over lower-elevation locations; meanwhile, they clearly realized that the average amplitude of stellar-image motion $\sigma \sim 0.3$ arcsec at zenith was related only indirectly to the long-exposure image quality.

Such a situation has forced us to study the site characteristics with the aim of optimizing future observations at the telescope that will be installed there.

The modern way to measure OT is based on the theory of wave propagation through an inhomogeneous medium and is focused on determination of the refraction-index structural constant C_n^2 . In typical conditions for night-time astronomical observations, one can make use of the linear weak-perturbation approximation where an atmospheric layer produces wavefront distortion independently from other layers (Tatarskii 1967; Roddier 1981). This simplification becomes invalid only in unusually strong OT conditions. The

^{*}E-mail: victor@sai.msu.ru

applicability of the Kolmogorov model of OT on scales of 0.01–3 m has been verified many times, while in the 3–30 m domain the von Karman model is normally preferred (Tokovinin, Sarazin & Smette 2007).

A number of methods to measure the altitude C_n^2 distribution, like Scintillation Detection and Ranging (SCIDAR; Fuchs, Tallon & Vernin 1998), Slope Detection and Ranging (SLODAR; Wilson 2002), Low Layer SCIDAR (LOLAS; Avila et al. 2008) and Lunar Scintillometer (LUSCI; Tokovinin, Bustos & Berdja 2010), were developed that are suited for particular measurement ranges. Meanwhile, the most representative and homogeneous OT data series were accumulated with the Differential Image Motion Monitor (DIMM; Sarazin & Roddier 1990) and Multi Aperture Scintillation Sensor (MASS; Kornilov et al. 2003) techniques, for which particular mention should be made of the large-scale site-selection programmes of the Thirty Meter Telescope (Schoeck et al. 2009) and the Extra Large Telescope of the European Southern Observatory (Vernin et al. 2008).

We formulated the main goal of our study as the collection of statistically reliable data on the seeing and altitude OT distribution during a 2–3 yr campaign. In parallel, representative information on the amount and quality of clear night sky, atmospheric transparency, sky-background brightness and on-site weather parameters had to be accumulated.

In the current paper we describe the instrumentation developed and the results of two years of site monitoring. Detailed data analysis and discussion of the results will be presented later. The next two sections provide a general description of the site selected to build the observatory, followed by the automatic site-monitor composition. Section 4 presents the two-year statistics of the main weather parameters: temperature, wind speed and direction and clear-sky data. Afterwards we recall the basics of the MASS and DIMM methods and describe some details of their implementation.

Section 6 is dedicated to the observation procedure and describes the measurement campaign performed at Mt Shatdzhatmaz. After this we list some data reduction features and particularities. The last section summarizes the main OT measurement results and compares them with the characteristics of other observatories. Finally, concluding remarks and some perspectives are given.

2 GENERAL SITE DESCRIPTION

A location for installation of the 2.5-m telescope was selected near the 2127-m top of Mt Shatdzhatmaz (Karachay–Cherkess Republic of Russia, 20 km southward from Kislovodsk), approximately 700 m to the south-east of the Highland astronomical (solar) station of Pulkovo Observatory. The mountain belongs to the Skalistiy (‘rocky’) ridge, which is parallel to the main Caucasus Ridge ~ 50 km away. As it gradually increases its height, the Skalistiy ridge approaches Mt Bermamyt (with a 2642-m summit) some 20 km to west of our site. In the opposite (south-east) direction, the ridge declines but has a prominent side extension in the form of a high plateau with the 2880-m Western Kinzhal top, 18 km away from the selected site.

This relief causes the western and northern winds to blow along a more-or-less flat surface, while south-eastern winds cross the deep (some hundred m) valley of the Hasaut River on the way from Kinzhal to Shatdzhatmaz. These circumstances significantly influence the local climate and atmospheric-turbulence characteristics, something that was also noticed by Gnevysheva (1991).

The 2.5-m telescope tower will be erected some 40 m from the steep south-east slope of the mountain ($+43^\circ 44' 10''\text{N}$, $+42^\circ 40' 03''\text{E}$), at elevation 2112 m from sea level (Fig. 1). Smaller instruments are planned along the ridge to the north-east of the 2.5-m telescope tower. The light-pollution situation is moderately good: the southern horizon is free from significant sources while there is a glow from towns of the Caucasus Mineral Waters region at the northern side. The Kislovodsk–Dzhily Su (northern Elbrus) road passes half a kilometre to the east of the observatory.

Some 100 km to the west, at the northern spurs of the main ridge, lies the Special Astrophysical Observatory of the Russian Academy of Sciences (SAO RAS), while the Terskol Observatory of the Institute of Astronomy of the RAS is located 50 km to the south. Unlike the selected site, both observatories are situated close to higher peaks.

Climatic parameters of our site are derived from the data for the meteorological station ‘Shatdzhatmaz’ located 600 m northward of the 2.5-m telescope tower. The year-averaged temperature equals $+2.3^\circ\text{C}$, while the daytime average temperatures vary from -6°C



Figure 1. Left: map of the local relief (sides are ca. 2 by 2.5 km). (1) automatic site monitor of SAI, (2) 2.5-m telescope mark, (3) Mt Shatdzhatmaz top, (4) Pulkovo solar station. Right: view of the automatic site-monitor facility at Mt Shatdzhatmaz from the south-west with a lab car to the left.

in winter to $+12^{\circ}\text{C}$ in summer. The mild local climate makes temperatures below -15°C and above $+20^{\circ}\text{C}$ very rare. The Caucasian humidity is more pronounced in summer (the average RH is 80–85 per cent), while in winter the weather is frequently dry (~ 65 per cent). The ground wind is breezy as a rule, although storms exceeding 35 m s^{-1} do happen from time to time. The surface consists of alpine meadows covered with non-deep snow in winter, which provides the low temperature contrast between day and night. The weather parameters we collected at the summit (see Section 4 later) are in agreement with these statistics.

3 AUTOMATIC SITE MONITOR

It is well understood that statistically reliable data on OT and other site characteristics are only obtained in the course of regular observations over a long (minimum 2–3 yr) time span. An optimal solution for this task is to install an automatic site-testing monitor that functions with no regular operator intervention. The need for such a robotic facility is supported by both our own experience at Mt Maidanak (Kornilov et al. 2009) in Uzbekistan and our colleagues' practice.

As a first step, we have developed a suite of automated instrumentation and software for measurement and accumulation of statistics on seeing, altitude OT distribution, clear-sky periods, atmospheric transparency and minimal weather parameters (speed and direction of ground wind, temperature and relative humidity). In this development we have benefited from the experience of similar studies at Cerro Tololo, La Silla, Cerro Paranal and other summits in Chile (Tokovinin et al. 2003a; Riddle, Schoeck & Skidmore 2006; Schoeck et al. 2009).

3.1 Equipment

The automatic site monitor (ASM) of SAI was installed at Mt Shatdzhatmaz in the summer of 2007, 40 m to the south-west of the spot reserved for the 2.5-m telescope. The first remote seeing measurements were conducted in 2007 October.

The heart of the monitor is the combined MASS/DIMM instrument attached to the automated amateur-class 12-inch telescope Meade RCX400. The telescope and instrument are run by a dedicated computer. This equipment is powered only during observations to assure detector safety and to minimize power consumption.

The telescope is mounted on a concrete 5-m high pillar with a $0.5\text{ m} \times 0.5\text{ m}$ section; thus its tube is at 6 m elevation above the ground. Such a height is typical for DIMM facilities at observatories; the 2.5-m telescope primary mirror will also have a similar elevation.

The telescope is protected by a custom-made enclosure with wooden side walls to minimize thermal effects (Fig. 1). The roof (dome) of the enclosure is constituted by steel arches with a tough waterproof fabric pulled over which are moved by a couple of electric actuators. When fully opened, the enclosure allows stars with zenith distances up to 65° to be reached. The enclosure is mounted on a metallic tower composed of three triangles made of 80-mm pipes fixed in three individual concrete foundations. Such a rigid construction vibrates quite moderately even at winds exceeding 20 m s^{-1} . The observation floor is accessed using a lightweight removable ladder.

Apart from the OT measurement equipment described, there is another compact computer located in the enclosure. It runs days and nights and handles the dome operations, the Wi-Fi link (IEEE 802.11b) with a router at the solar station, the equipment power

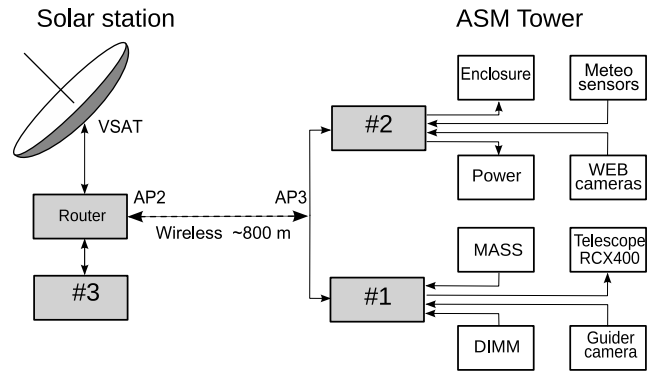


Figure 2. The network ASM structure. #1: OT measurements computer; #2: infrastructure control and meteo data-acquisition computer; #3: observation management, data storage and http server.

management and the collection of weather data. Two survey webcams are also driven by this machine in order to control the telescope and outdoors area. Meteorological instruments (an anemometer and temperature (T) and relative humidity (RH) sensors) are fixed at 5 m height on a special mast atop the lab car roof.

The ASM power is supplied by storage batteries with a 400 A h total capacity. This provides 7–10 d of operation, as the permanently running part consumes about 20 W and the night-time observation equipment needs 40 W in addition.

It should be admitted that technical problems affected our site testing over a rather long period, so completely automatic operation only began in February 2008. The major issues were related to the RCX400 scope, which is not very suitable for an autonomous work, having a number of drawbacks and some bugs in its firmware. Also, battery-charging was problematic until the summer of 2008, causing interruptions in the observations.

3.2 Network and software architecture of ASM

In Fig. 2 we illustrate schematically the communication structure for ASM. One can see that it is based on three linked computers controlling the hardware. All computers are running free software under the GNU/Linux OS. Data from the custom-made equipment (MASS instrument electronics, meteo controller, dome and power-management units) flow via serial RS485 interfaces.¹

Apart from those described above, there is a computer (number 3) in the solar-station communication room which controls observations and serves as data storage. Also, it runs an http server² which allows control of the ASM state via the internet.

The main software consists of a number of independently running applications that communicate with each other via TCP/IP connections. Division of the ASM software into independent components allowed us to gain in system flexibility, to maintain the overall system stability and to simplify considerably the logic of each application. The programs are normally running in background as *daemons*.

Each application accomplishes a separate ASM logical task or function, e.g. the TLSP program provides telescope pointing, object centring and guiding during measurements, for which it communicates with the scope and a finder camera.

¹ http://curl.sai.msu.ru/mass/download/doc/new_details.pdf

² <http://eagle.sai.msu.ru>

The programs are all running as servers, processing only external command requests. An exception is the weather-data collecting program MONITOR, which starts to poll the meteo controller and to store the results in an output file immediately after start-up. Meanwhile, it also provides server functions, giving information on actual conditions when requested.

A simple protocol was implemented³ for inter-program communication. The commands are given in text (ASCII) form, which also allows manual operation of the program components using a system telnet utility while debugging or troubleshooting.

In the automatic mode of operation, the programs are controlled by the supervising program AMEBA running on computer 3, which generates client requests to the programs. It provides the logic of the ASM operation according to the algorithms detailed in Section 6.

4 WEATHER PARAMETERS AND CLEAR-SKY STATISTICS

A minimal set of meteo sensors was included in ASM in order to (i) provide safe autonomous operation and (ii) accumulate a homogeneous data set on weather conditions that is also useful for a subsequent analysis of OT monitoring results. No attempt to standardize (calibrate) the measurements strictly was performed. The T , RH and wind sensors are read out by the MONITOR program with a 2-s sampling time to provide instantaneous values that are on-the-fly averaged into less noisy 1-min values.

4.1 Clear night sky

The clear skies have been monitored since summer 2006 using the Boltwood clouds sensor⁴ which is connected to a server of the MASTER project (Lipunov et al. 2010) at Pulkovo solar station. This bolometric sensor measures infrared radiation of the sky in the spectral range 5–10 μm , which gives the brightness temperature of the sky. Clear-sky statistics were computed from the 3-yr data set spanning the period 2006 November 20–2009 October 31. The sky was ranked clear when $\Delta T = T_{\text{sky}} - T_{\text{amb}} + T_{\text{sen}} < -22^\circ\text{C}$ (where T_{sky} , T_{amb} and T_{sen} are temperature readouts from the cloud sensor). This criterion is illustrated by the nautical night-time ΔT distribution in Fig. 3, where the left peak reflects the clear-sky condition.

Since there are astronomical observations that are not critical to the sky background, we expanded the clear-sky analysis to include two conditions: astronomical night (sun altitude $h_{\odot} < -18^\circ$) and nautical night ($h_{\odot} < -12^\circ$). In Fig. 4 the diagram of the clear nautical night-sky distribution is shown for the above specified 3-yr period.

The annual amount of clear astronomical night sky at Mt Shatdzhatzmaz is 1343 h, compared with the theoretical total of 2950 night-time hours at the given latitude. This amount is slightly higher than the Rylkov & Bobylev (1991) estimate of 1200 h. For nautical nights, the annual amount is 1546 h, while the calculated total is 3451 h.

The monthly clear-sky astronomical and nautical time distribution is given in Table 1. It shows that the most favourable observation period is from mid-September to mid-March, containing ≈ 70 per cent of the yearly total clear-sky hours. This period coincides with the time of the slowest high-altitude wind.

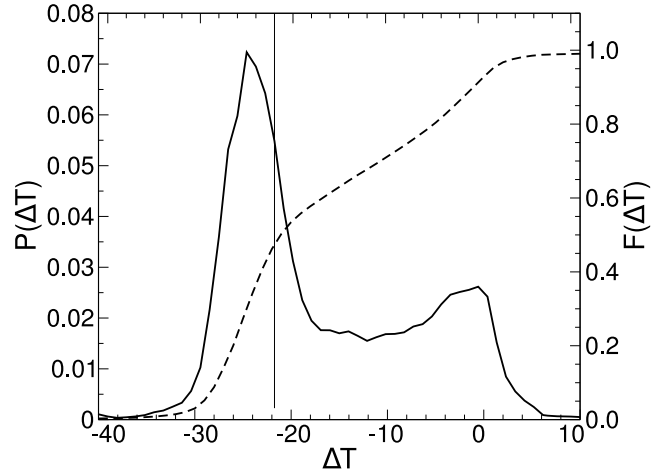


Figure 3. Differential (solid line) and integral (dashed line, right axis) distributions of ΔT in nautical nights. The thin vertical line depicts the selected threshold used for clear-sky detection.

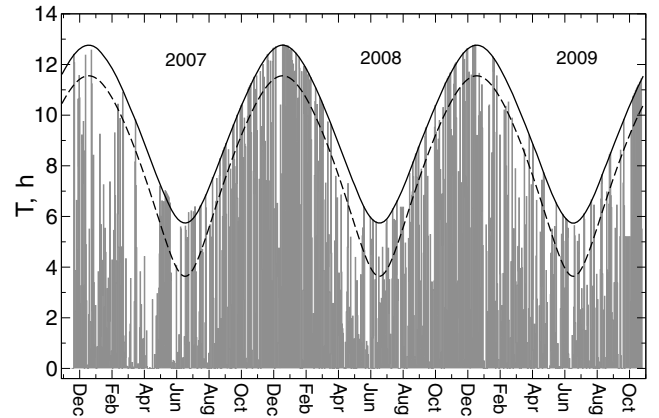


Figure 4. Clear-sky nights distribution 2006 November 20–2009 October 31. The solid line denotes the nautical night duration, the dashed line the astronomical night.

The direct comparison of clear night hours between observatories is complicated by differing clear-sky criteria and the way the data are presented in terms of fractions of the whole night. However, for Maidanak, La Silla and Paranal observatories the annual clear-sky night-time (Table 2) is recalculated from the data of Ehgamberdiev et al. (2000). The estimation of the SAO clear skies is reported by Leushin et al. (1975). We derived the clear sky for the Terskol peak using the 0–2 cloudiness data from the paper of Depenchuk, Kondratyuk & Kojfman (1977). In the latter study, the authors give a yearly clear-sky duration of 1200 h, including partially clear weather.

The ΔT criterion given above is rather strict; it was chosen to avoid frequent ASM shut-downs due to lowering of measured star counts. Such a threshold corresponds to the conditions that other authors refer to as ‘photometric skies’. Softening the threshold to, say, $\Delta T = -18^\circ\text{C}$ (corresponding to cloudiness ≈ 25 per cent) boosts the clear night fraction from 46 to 58 per cent.

4.2 Temperature

The outside temperature sensor is based on the TMP36 circuit (Analog Devices) and is installed in a standard meteorological hous-

³ See http://curl.sai.msu.ru/mass/download/doc/sv_ug.pdf

⁴ <http://www.cyanogen.com/fix.php>

Table 1. Monthly amounts of astronomical and nautical clear night sky CS (in hours) and its fraction relative to the total night-time (in per cent).

Month	Astronomical		Nautical	
	CS	Frac.	CS	Frac.
Jan	158	45	175	46
Feb	131	44	145	46
Mar	85	31	95	31
Apr	45	22	53	21
May	62	40	80	38
Jun	44	39	64	36
Jul	58	42	82	42
Aug	79	40	94	39
Sep	101	41	116	41
Oct	189	62	210	62
Nov	197	60	216	60
Dec	193	54	213	54

Table 2. Annual clear astronomical night sky at six observatories: actual clear sky (in hours), fraction of the total night-time (in per cent) and total night-time (in hours).

	Clear sky	Fraction	Whole
Shatdzhatmaz	1343	46	2950
SAO	1020	34	2961
Terskol	874	29	2975
Maidanak	1697	55	3088
La Silla	1861	57	3291
Paranal	2604	78	3350

ing in order to minimize heating by the Sun. A comparison of its reading with data from the cloud sensor and the meteo station records showed the discrepancies to be below $\pm 2^\circ\text{C}$.

Although our weather data accumulation was started on 2007 July 19, the analysis encompasses the period starting from 2007 November 1. The absolute range of temperatures on clear nights is from $+17.8^\circ\text{C}$ to -17.2°C . The median value is $+1.8^\circ\text{C}$, which is more typical for observatories at higher altitudes.

Low temperatures on clear nights reduce the typical precipitable water vapour. Obtained from processing of the GPS signal wet-delay data, the water content shows a median value of 7.75 mm. A detailed study of the precipitable water vapour and optical extinction above the summit will be published elsewhere.

As a comparison, the yearly average temperature at SAO we derived using the weather-page data from the observatory website⁵ is $+4.2^\circ\text{C}$ over the same period. When weighted by the observation-time distribution, it might be even higher, since the summer–autumn is the favoured observing season there. At the Terskol site, the yearly average temperature weighted by observing time is -6.1°C .

In Fig. 5 we present a diagram of night- and daytime temperatures averaged within months. The first and third quartiles Q_1 and Q_3 of the monthly distributions are plotted for reference. It is clear that the two-year data span is not long enough to obtain statistically reliable monthly averages.

The local turbulence is largely dependent on the contrast between the day- and night-time temperatures. At our site, the diurnal temperature difference is small and amounts to 1.3°C if computed as

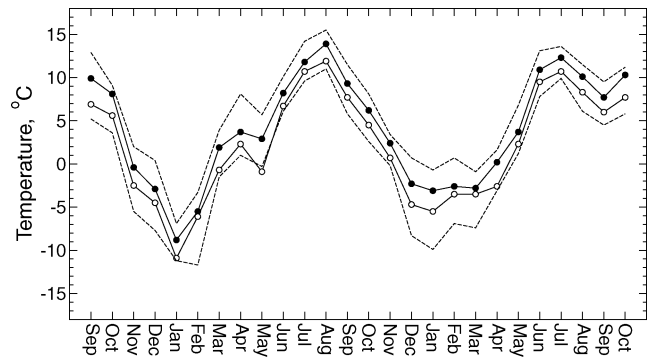


Figure 5. Two-year evolution of the monthly median daytime (black filled circles) and night-time (open circles) temperatures. Dashed lines trace the first and third quartiles of the monthly distributions.

the difference of temperatures 1 h before and 1 h after sunset. If one takes the full amplitude of daily variation between noon and midnight, then it becomes $\approx 3.4^\circ\text{C}$ for those days when the following night was clear.

A similar diurnal temperature variation is observed at SAO RAS, where the surface character is similar. At Terskol, the average difference is $\approx 2.9^\circ\text{C}$ as quoted by Depenchuk et al. (1977). These contrasts were computed for the entire data set, without regard to cloudiness.

4.3 Ground wind speed

The strength and direction of ground winds define the airflow conditions about the local relief and the observatory and influence the generation of ground-layer turbulence.

Wind speed and direction were measured using a conventional cup anemometer by Davis Instruments (model 7911) attached to the meteo controller. Our data show that the wind at the summit is mostly a light breeze, in agreement with the official meteo statistics. In Fig. 6 the monthly median values of the night- and daytime wind speed are shown accompanied by the respective quartiles of the distributions. It is noticeable that the night wind is more stable throughout the year while the daytime wind is stronger in summer.

The global median wind speed is 3.3 m s^{-1} in the daytime and 2.3 m s^{-1} at night, both for clear and cloudy scenarios. Similar values are characteristic for the Maidanak summit (Ehgamberdiev et al. 2000), which was identified as an advantage over many other observatories. Meanwhile, in 1 per cent of cases the wind is stronger

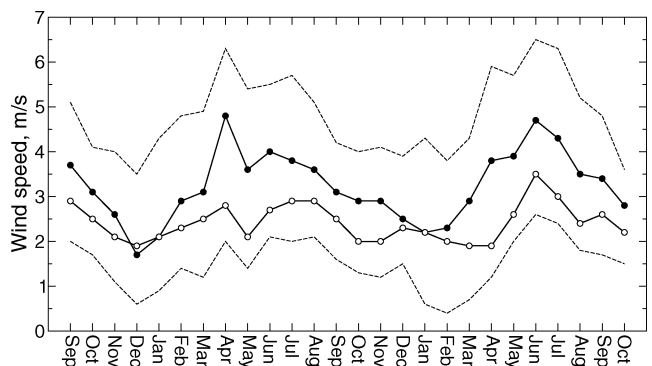


Figure 6. Two-year evolution of the monthly median wind speed during daytime (black filled circles) and night-time (open circles). Dashed lines depict the first and third quartiles of the monthly distributions.

⁵ <http://www.sao.ru/tb/tcs>

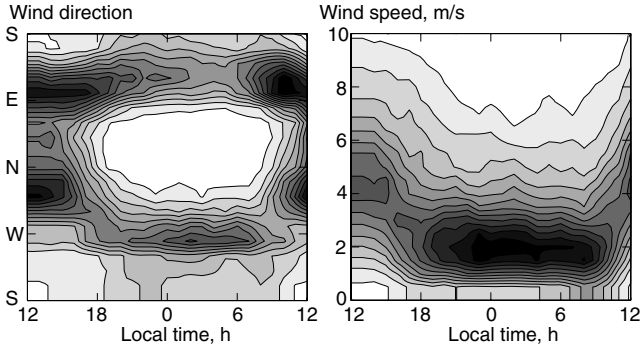


Figure 7. Two-dimensional probability distribution of the direction (left) and strength (right) of wind as a function of the local time. Midnight is in the middle, more dense (darker) regions correspond to higher probability.

than 12 m s^{-1} . In the night-time a strong wind is rare; wind speeds in excess of 9 m s^{-1} occur in 2.2 per cent of cases. The dependence of wind speed on the time of day is shown in Fig. 7.

The dominant wind direction at night is mostly from the west and, to a smaller extent, from the south-east. The midday behaviour is different, as north-westerly winds become more frequent. The probability distribution of the wind direction as a function of time of day is shown in Fig. 7 (left). Apparently, preferred wind directions are related to the large-scale relief properties.

The National Centers for Environmental Prediction/National Center for Atmospheric Research (NCEP/NCAR)⁶ data base is a recognized standard source of high-altitude wind data. According to it, for most of the year (October–May) the wind speed at 13 km altitude is about 20 m s^{-1} , while in summer (June–September) it increases to 35 m s^{-1} . This is expected, since the Shatdzhatmaz latitude corresponds to the minimum between the tropical and polar streams. The situation is similar at other moderate-latitude observatories (Carrasco, Avila & Carramiñana 2005).

For comparison, analysis of the weather data at SAO for the 2007–2009 period shows the median/mean night-time wind speed to be $2.0/3.8 \text{ m s}^{-1}$ in winter and $1.3/2.3 \text{ m s}^{-1}$ in summer. Meanwhile, the probability of strong ($>9 \text{ m s}^{-1}$) winds is 0.13 and 0.04, respectively. Nelyubin & Vasilyev (1969) report a slightly different situation with 5.9 m s^{-1} during October–March and 2.5 m s^{-1} during April–September recorded in the 1960s. Similarly to SAO, the winds at the Terskol peak are stronger in winter than in summer: $2.5\text{--}3.6 \text{ m s}^{-1}$ and $1.4\text{--}2.6 \text{ m s}^{-1}$, respectively.

5 OPTICAL TURBULENCE MEASUREMENT

5.1 The principles of MASS and DIMM instruments

Let us recall that the OT power is described by a single parameter in the Kolmogorov model. This is normally the Fried radius r_0 (atmospheric coherence radius). Meanwhile, a more appropriate measure for description of the turbulence distribution along the line of sight is the turbulence intensity J (having the dimension of $\text{m}^{1/3}$), which is defined as

$$J = \int C_n^2(z) dz, \quad (1)$$

where the integration is performed along the whole light path. J is related to the Fried radius as

$$J = 0.06 \lambda^2 r_0^{-5/3}, \quad (2)$$

or

$$J = 1.5 \times 10^{-14} r_0^{-5/3} \quad \text{if } \lambda = 500 \text{ nm}. \quad (3)$$

Unlike other parameters, J is additive and does not depend on wavelength. In order to compare the measurements performed at different air masses M , one should reduce the measured J' to zenith, where the light-propagation distance z is replaced by height h : $J = J'/M$.

It is more common to quantify the full turbulence at a given site by the image quality β (seeing), which has the sense of a characteristic size of the turbulent disc (full width at half-maximum (FWHM)) registered with a long exposure in a large ideal telescope. For $\lambda = 500 \text{ nm}$ this measure (in arcsec) is

$$\beta = 2 \times 10^7 J^{3/5}. \quad (4)$$

The theory of the DIMM instrument is described by Sarazin & Roddier (1990) and Tokovinin (2002a). The principle is based on the measurement of the differential displacement of two star images constructed by two circular apertures. These apertures have diameter D about 10 cm each and are separated by a baseline distance d about 20 cm in the telescope-entrance pupil plane. The star images are offset from each other by additional optical elements.

Such a differential motion is described in terms of differential slopes of respective wavefront regions, related to the OT power. The variance of the longitudinal differential motion $\sigma_{l,t}^2$ (along the aperture baseline) and the transverse motion $\sigma_{t,t}^2$ (perpendicular to the baseline) is expressed as

$$\sigma_{l,t}^2 = 16.7 K_{l,t} D^{-1/3} J. \quad (5)$$

Equation (5) is obtained from a conventional expression from the above-cited papers by the substitution of r_0 from formula (3).

For the Kolmogorov turbulence spectrum, the coefficients $K_{l,t}$ depend solely on the aperture geometry (Sarazin & Roddier 1990):

$$K_l = 0.358 [1 - 0.541 (d/D)^{-1/3}], \\ K_t = 0.358 [1 - 0.811 (d/D)^{-1/3}]. \quad (6)$$

Thus the DIMM sensor allows researchers to measure the full OT intensity from the telescope entrance to the upper boundary of the atmosphere. This is essential, but still insufficient, information.

MASS (Kornilov et al. 2003) is a technique allowing us to obtain detailed information about the OT vertical distribution. This method is based on simultaneous measurements of stellar scintillation in four concentric entrance apertures. This allows us to obtain four normal and six differential scintillation indices s^2 , which are the variances of relative light-intensity fluctuations. Scintillation is measured with 1 ms exposure and s^2 are computed for 1-s time intervals (Kornilov et al. 2003; Tokovinin et al. 2003b, hereafter TKSv).

Weak perturbation theory implies that scintillation indices s^2 are produced by the whole atmosphere in the following way:

$$s^2 = \int_0^\infty C_n^2(z) Q(z) dz, \quad (7)$$

where $Q(z)$ is a weighting function depending on the wave-propagation geometry: the entrance-aperture dimensions and angular size of a source. For the particular instrument geometry and assumed spatial spectrum of scintillation, the weighting function can be computed theoretically (Tokovinin 2002b; TKSv).

⁶ <http://www.esrl.noaa.gov/psd/data/reanalysis/reanalysis.shtml>

Having 10 equations like (7) with different weighting functions, one can solve the inverse problem and obtain the OT profile from the measured indices s^2 . For a feasible set of entrance apertures (defining a respective set of $Q(z)$) the problem is ill-conditioned so the non-trivial procedure of vertical-profile restoration constitutes a key part of the MASS technique (TKSV; Kornilov & Kornilov 2010). The main drawback of the scintillation method is its blindness to the ground-layer turbulence, so without additional measurements in this important domain the results can suffer from considerable incompleteness.

5.2 The combined MASS/DIMM instrument

Since the MASS apertures can be inscribed in a ~ 10 cm circle, both MASS and DIMM methods may be implemented in a single instrument fed by a 10–12 inch telescope. This was realized in late 2003, and the details of the construction of this combined device and its properties are discussed by Kornilov et al. (2007). The advantages of this approach are obvious: one needs a single telescope; a DIMM-channel camera serves for centring and guiding of a star; both methods deal with the same volume of turbulent atmosphere so that its non-stationary nature does not prevent the joint analysis of data. These devices were involved in the majority of large-scale site-testing campaigns over the last few years (Vernin et al. 2008; Schoeck et al. 2009).

Our instrument differs by the model of the DIMM channel detector. A high-speed industrial CCD camera EC650 from Prosilica with Firewire interface (IEEE1394) is used. The camera fully complies with the IIDC standard, so the open library LIBDC1394⁷ may be used to program the data exchange under the GNU/Linux OS.

Setting the exposure time to 4 ms allows us to achieve an image rate of ≈ 200 frames per second in the region of interest (ROI), 60×100 pixels – much faster than with other cameras used in DIMMs. Such a frame rate allows us to measure the variances $\sigma_{i,t}^2$ with the maximal possible accuracy. The low readout noise of $\approx 10e^-$ allows us to use stars up to fourth magnitude.

An important calibration parameter of DIMM is the pixel scale of the detector, since $\sigma_{i,t}$ in equation (5) must be in radians. Initially we estimated the scale in a conventional way with help of the visual double star HR7141/2 = θ Ser, which has a 22.3-arcsec separation. The diurnal sky rotation appeared to provide us with a more convenient and precise way to calibrate the scale, delivering a value of 0.612 arcsec pixel⁻¹. The entrance-aperture dimensions d and D are set by the physical sizes of the DIMM mask, which is located in the exit pupil of the ‘telescope+instrument’ system, and by the magnification k of this system. The d/D ratio was measured as 2.18 ± 0.02 ; the aperture sizes D were both 90 mm.

The OT-profile restoration is based on precise knowledge of weight functions (7), which also depend on the system magnification k determining the effective sizes of entrance apertures. Therefore each focusing of the Fabry lens was followed by the measurement of k with 1–2 per cent precision ($k = 16.3$ in the final state). Since functions $Q(z)$ also involve chromatic effects and thus depend on the spectral response of MASS detectors, the latter was controlled⁸ by special observations of stars with a wide range of colours, similarly to the technique of Kornilov et al. (2009).

The MASS-channel data reduction also requires other instrumental parameters, namely the detectors non-Poissonity p and non-

linearity τ , which serve to correct exactly for the photon-noise contribution to measured variances (Kornilov et al. 2003). These parameters were also monitored using dedicated measurements.

5.3 MASS/DIMM control and data acquisition

Unlike the service applications described in Section 3.2, the MASS/DIMM driving programs MASS and DIMM affect not only the overall ASM efficiency but the reliability of the results themselves.

The principal functionalities of the MASS program are almost the same as those of the preceding TURBINA program and are described in TKSv and Kornilov et al. (2007). The main difference is the absence of graphical user interface and real-time profile restoration, which proved to be a source of instability in the automatic and remote mode of operation.

The program performs continuous light-intensity recording in A, B, C and D apertures with an elementary integration time of 1 ms during a 1-s basic measurement. This data set is processed on-line in order to compute different statistics: variances and covariances with time lag 1 and 2 for normalized signals and their combinations. These statistics are stored in the output file for subsequent processing.

Measurements are started by an external command and repeated over an accumulation time. The mentioned integration, basic and accumulation times, along with other parameters specifying the measurement process, are read by the program from a configuration file during initialization. No command can change these settings, which ensures the good homogeneity of output results.

The DIMM program for communication with the DIMM-channel camera has a similar functional structure. Each subframe obtained from the video stream (containing the image of the ROI) is processed to recognize two stellar images for which the gravity centres and other characteristics are computed. The frame exposure, measurement time and accumulation time are also defined by a configuration file.

A special command initiates the measurement of the star position in a full frame when searching for a new target and starting guiding.

6 OBSERVING CAMPAIGN

6.1 The RCX400 telescope peculiarities

Remote and automatic observations demand a pointing accuracy of about 1 arcmin in order to get a target well inside the MASS/DIMM field diaphragm with an ≈ 2 arcmin radius. Such an accuracy is achievable with RCX400 after one determines the telescope coordinate system using the three-stars method. Meanwhile, bugs in the instrument firmware cause the telescope controller to lose this reference occasionally, while its remote recovery does not provide the needed precision.

To cope with this situation, we attached a web camera (Philips SPC900NC) to the telescope finder, which allows us to detect stars up to eighth magnitude in the $0.9 \times 1.2^\circ$ field of view. The TLSP program uses images from that camera to search, centre and guide targets. However, accurate guiding during OT measurements is made using the DIMM-channel information.

Introduction of a CCD finder and development of optimized procedures to restore the telescope coordinate system after powering it on and to control the axis movement explicitly while slewing solved the pointing problem. More than 3500 successful pointings were performed during the campaign.

⁷ <http://damien.douxchamps.net/ieee1394/libdc1394/>

⁸ http://curl.sai.msu.ru/mass/download/doc/mass_spectral_band_eng.pdf

Another major RCX400 problem is its focusing, which gradually deteriorates the optical adjustment (so-called collimation). The accumulating tilt errors of the secondary mirror produce a coma, which is seen as astigmatism in the DIMM apertures, biasing measurements of OT strength (Tokovinin & Kornilov 2007). Meanwhile, the documented collimation procedure can only be performed interactively. Only in the autumn of 2009 did we overcome this restriction.⁹

In general, the ‘telescope+DIMM’ optical system was maintained in a good state. The quality was controlled by the Strehl ratio S of the DIMM images; its median value over the whole campaign was 0.47 for both apertures.¹⁰ Only in the period from 2009 April–June was the telescope alignment worse, and S progressively decreased to 0.3 (left image) and 0.2 (right image). At most 5 per cent of measurements were performed in this state.

Another annoyance was dew condensation on the telescope corrector plate in windy and humid conditions. Invention of a special-shape dew cap in 2007 November allowed us to get rid of this problem.

An additional factor limiting the measurement ability is wind-caused telescope vibration. In slow wind conditions, the common image motion is about ± 0.5 arcsec and is caused mainly by cophased turbulence effects and telescope-tracking errors. With the wind speed in excess of 3 m s^{-1} , the vibration amplitude grows almost linearly and approaches 10 arcsec in elevation when the wind is $7\text{--}8 \text{ m s}^{-1}$. The amplitude in azimuth is half of this. The wind gusts excite several telescope eigenmodes near 10 Hz, so the vibration amplitude may eventually exceed 20 arcsec. In this case the ROI must be enlarged and the frame rate becomes slower.

More importantly, in these conditions the images are moving so quickly ($>600 \text{ arcsec s}^{-1}$) that the respective smearing exceeds 2.4 arcsec during exposure. As in the optical-aberration case, this effect introduces DIMM measurement errors and biases the OT estimations toward strong high turbulence. Luckily, 97 per cent of measurements were made with vibration amplitudes below 6.4 arcsec and 85 per cent with amplitudes <3 arcsec.

6.2 Operation control and time coverage

Control of the ASM is performed by the AMEBA program, which is started daily in the evening at computer 3 and communicates with the respective servers.

OT measurement is initiated when the following conditions are fulfilled: (1) the sun altitude is below -12° ; (2) the cloud sensor reports clear sky; (3) the wind speed does not exceed some limit; (4) the battery voltage is normal. Humidity was not decisive because of the odd sensor behaviour near the dew point, when condensing moisture induced an abrupt lowering of the sensor reading.

When all conditions are satisfied, an observation session is started consisting of the following stages.

(i) Dome opening, powering up the observation equipment, TLSP, DIMM and MASS program initiation.

(ii) Target selection from a list¹¹ of 119 bright stars according to magnitude, altitude, distance to the Moon and available measurement duration.

(iii) Pointing to the target followed by its search, centring, brightness check and guiding start-up.

(iv) Background measurement in the MASS channel, performed before and after target measurements.

(v) In the case of failed pointing or high background, another target is selected.

(vi) The target measurement session is performed for 1.5 h or until one of the selection criteria is violated.

(vii) In the case of an error during measurement (equipment failure, stellar-flux drop) another target is selected.

(viii) If an error occurs three times in row, the session is finished; the dome is closed and the equipment is switched off.

After the session is finished by worsened conditions, AMEBA waits for restoration. In order to prevent random effects, hysteresis is introduced. For example, observations stopped by a wind speed in excess of 9 m s^{-1} will be resumed after the wind speed remains below 6 m s^{-1} for 20 min. Such a pause is obligatory after any session is stopped by an error. Note that the system initialization and parking lasts 2–3 min. At the end of the night, AMEBA stops condition-checking or a measurement session and shuts itself down.

In the course of a few months after the campaign’s start, we were operating ASM remotely while simultaneously developing and testing the automatic operation algorithms. This period supplements 10 per cent of the data. Fully automated observations were started in 2008 February.

In Fig. 8 the duration of nightly measurement sessions is plotted for every calendar date of the whole campaign. The total observation duration defined as the sum of time spans between dome opening and closing and is 1753 h. The net measurement time is 1485 h or $\approx 90\,000$ OT determinations, while about 18 per cent of the time was spent on service operations: pointing, centring, background measurements etc. In 2009 October the observation sessions lasted longer than nautical nights, since experimental twilight observations were introduced.

In Table 3 we list the total monthly measurement duration for the whole period of the campaign. One should be aware that nights were counted as ‘observational’ when even a single successful OT measurement was performed.

The E column reflects the efficiency of the clear-time use and characterizes the gradual decrease of technical problems. The global efficiency for the whole period is 0.49.

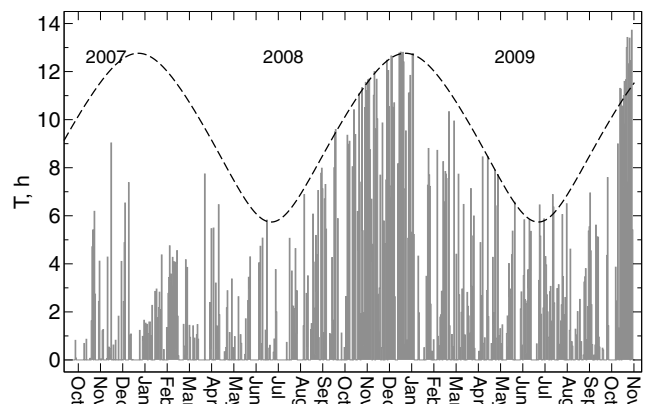


Figure 8. Duration of measurement plotted for the whole period of ASM monitoring. The dashed line is the nautical night duration ($h_{\odot} < -12^\circ$).

⁹ See http://curl.sai.msu.ru/mass/download/doc/rcx_advices.pdf

¹⁰ http://curl.sai.msu.ru/mass/download/doc/shtrel_controls.pdf

¹¹ http://curl.sai.msu.ru/mass/download/doc/new_mass_cat.pdf

Table 3. Monthly duration of measurements in nights (n) and hours (h) in 2007–2009. Efficiency (E) is given in per cent.

Year Month	2007			2008			2009		
	n	h	E	n	h	E	n	h	E
Jan	–	–	–	19	36	12	14	63	44
Feb	–	–	–	21	57	26	17	83	79
Mar	–	–	–	11	24	18	19	60	63
Apr	–	–	–	14	31	48	19	65	82
May	–	–	–	10	20	39	15	40	63
Jun	–	–	–	13	33	54	18	64	83
Jul	–	–	–	10	23	30	22	68	92
Aug	–	–	–	20	75	72	20	47	48
Sep	1	1	1	15	64	58	15	40	52
Oct	10	29	13	23	174	85	18	192	97
Nov	11	24	11	24	187	85	–	–	–
Dec	13	30	13	27	220	88	–	–	–

7 OT-MEASUREMENT DATA REDUCTION

7.1 Features of the reduction and its modifications

Conventional DIMM data processing is quite simple: turbulence intensity J is computed directly using equation (5) after longitudinal and transverse variances are converted from pixels to radians. Then J is reduced to zenith and expressed as seeing β if necessary.

Meanwhile, there are a number of features that upset this simplicity. The first is finite exposure, which suppresses the high-frequency part of the differential image motion. This effect becomes apparent for strong winds in the boundary layer, where the main part of the turbulence is usually located, and at high altitudes with wind streams of 25–40 m s⁻¹. It is common to use a double-exposure method when frames of single and double exposures are interlaced, and a certain extrapolation (Tokovinin 2002a) is exploited to obtain a ‘zero-exposure’ variance estimation based on theoretical considerations (Martin 1987; Soules et al. 1996).

The use of high-speed cameras does not allow for this technique, since the exposure cannot be changed without stopping the video stream. Instead, the DIMM program calculates the covariance coefficient between the image coordinates in adjacent frames. Such an approach has been theoretically justified by V. Kornilov & B. Safonov.¹² Since the exposure is as low as 4 ms, the correction does not exceed 0.05 for 90 per cent of measurements.

A complementary feature is related to the low-frequency domain of the image-motion power spectrum. In order to make possible the joint analysis of MASS and DIMM data aimed at restoring the full OT profile, the DIMM measurement *basetime* has to be 1 or 2 s. In this case, part of the power produced by slowly drifting air in the ground layer escapes detection in the DIMM channel.

The low-frequency power is estimated using the variance of basetime-derived image separations computed over the *accum-time* span (normally covering 60 s), and this power is added to the basetime-derived results. This allows us to find a trade-off between a statistically reliable accumulation time and the process stationarity period and to ensure that the method detects a large fraction (>0.99) of the motion power.

The third issue is that equation (5) is valid only in the near-field approximation, i.e. when $D^2 \gg z\lambda$. This condition is not fulfilled in

practice and thus not all the high-altitude turbulence is measured due to wave propagation. This effect was evaluated (Tokovinin 2002a; Tokovinin & Kornilov 2007), but was ignored in practice because its correction implies knowledge of the OT distribution.

The MASS data processing is based on the solution of an equation set of the kind (7) for a fixed altitude grid under the restriction that the solution must be non-negative. This restriction regularizes the solution. The technique of OT vertical-profile restoration from scintillation indices and its features were described by Kornilov et al. (2007) and TKS_V.

Experience gained in previous MASS data processing has allowed us to modify significantly the algorithms and structure of the data-processing utility *ATMOS*, which was initially part of the *TURBINA* program. The non-linear minimization method was replaced by a much faster and mathematically proven non-negative least-squares method (NNLS). Also, OT-profile restoration by accutime-averaged scintillation indices was replaced by averaging the OT profiles restored from the 1-s data. Such an algorithm modification (*ATMOS-2.96.0A*) reduces the profile errors and leads to more physically justified turbulence characteristics (Kornilov & Kornilov 2010). Additionally, this permits restoration of an OT profile using a denser altitude grid for more accurate localization of the turbulence features. Quality of the profile restoration is controlled by the total residual R^2 , which is the accutime-averaged sum of squared residuals of indices.

A further modification (*ATMOS-2.96.7*) of the algorithm involves the DIMM data in the OT-profile restoration. A polychromatic representation of the DIMM weighting function $W_{1,t}(z)$ was deduced by V. Kornilov & B. Safonov¹² which, analogously to equation (7), allows one to relate the differential motion variance σ^2 to the refractive-index structural-coefficient distribution:

$$\sigma_{1,t}^2 = \int_0^\infty C_n^2(z) W_{1,t}(z) dz. \quad (8)$$

The new linear equation system is obtained from the original one for scintillation indices by the addition of two equations for longitudinal and transverse components of differential motion and by adding a zero-height point to the altitude grid.

As well as direct determination of the ground turbulence intensity, it is now possible to correct for propagation effects in the differential motion. Non-negativity of the ground-layer intensity also stabilizes the solution. A detailed description of the new algorithm and its features will follow.

It is important to note that DIMM weighting functions are calculated under the assumption that our DIMM measures differential motion that is better matched by an aperture-wavefront slope in the Zernike polynomial approximation, namely the so called z -*tilt*, rather than gravity-centre displacements (g -*tilt*), according to Tokovinin (2002a). This decreases the derived intensities slightly (by 3 and 5 per cent for longitudinal and transverse components, respectively) compared with those from equations (5) and (6).

7.2 Data filtering

The raw MASS data set contains 89 189 one-minute star measurements and 6544 background measurements (for 404 nights). When there are DIMM data for the same time intervals, they are included in the processing. For some periods they are unavailable, mostly in cases of excessive telescope vibration when a star escapes frequently from the ROI. In this situation no ground-layer restoration is performed.

¹² http://curl.sai.msu.ru/mass/download/doc/dimm_specs.pdf

Since the background level is involved in scintillation-index computation, it is essential to detect and reject cases when some star was present in the field aperture while the background was recorded. The program accepts the background measurement only if its variance is consistent with solely photon noise. Target measurements with intensities only marginally exceeding the background level are also rejected.

The data that have passed filtering (88 664 measurements) are used in OT-profile restoration and integral atmospheric parameter calculation. A residuals analysis is performed to clean out the outlying cases in the 1-s OT data set, which may affect the output statistics.

A further filtration was made while analysing the output results. Events of clouds, corrector-plate fogging, star escapes from the diaphragm, etc. were detected by the D-channel count dropping below 100 pulses ms^{-1} and by relative flux errors exceeding 0.05. The latter value is much more than the median 0.002 of the relative errors due to scintillation, so the derived statistics were not biased. These checks rejected 0.9 per cent of the data. Finally, extinction star measurements were thrown away if performed at an air mass higher than 1.38. MASS instrumental problems in the period 2009 July 19–23 were detected from abnormal C/D flux ratios.

The residuals analysis has demonstrated that including DIMM data in the profile restoration significantly increases the total residual R^2 (from 1.46 to 2.62 for the global median) in spite of the weak coupling of MASS and DIMM data. The reason was an inconsistency between longitudinal and transverse image-motion variance. When only one DIMM equation is included in the system (either l or t), the R^2 drops back almost to its original MASS-only level.

The distribution of residuals is similar to the one without DIMM data, but starting at $R^2 \approx 4$ it shows a prominent flat tail. In these cases the actual data come into severe conflict with the model. Inspection allows us to propose two main reasons: (1) sometimes MASS determines stronger turbulence than follows from the DIMM data, and (2) longitudinal and transverse components of the differential motion are mutually incompatible.

The first situation is discussed in a number of papers as an ‘overshoots’ or ‘negative ground layer’ problem and is considered in Section 8.3. Although we made some progress in treatment of such cases (see above), and they are encountered now quite rarely, they have not disappeared completely. The second issue became especially prominent in 2009 June due to optics misalignment, when the median residual grew up to ≈ 5 .

To filter out completely inadequate solutions, we adopted a threshold residual $R^2 = 12.4$ which corresponds to 0.5 per cent cases, which indeed appear to be marginal. By the end, a total of 85 512 OT measurements have passed all filters and are included in the statistics discussed below.

8 TURBULENCE MEASUREMENT RESULTS

8.1 Seeing statistics

Vertical OT distributions were restored on a logarithmic altitude grid of 13 layers at 0, 0.5, 0.71, 1, 1.41, 2, 2.82, 4, 5.66, 8, 11.3, 16 and 22.6 km above the observatory. This grid is based on the conventional MASS grid (see TKS_V) with intermediate and zero-height nodes inserted. As an example, in Fig. 9 we present processing

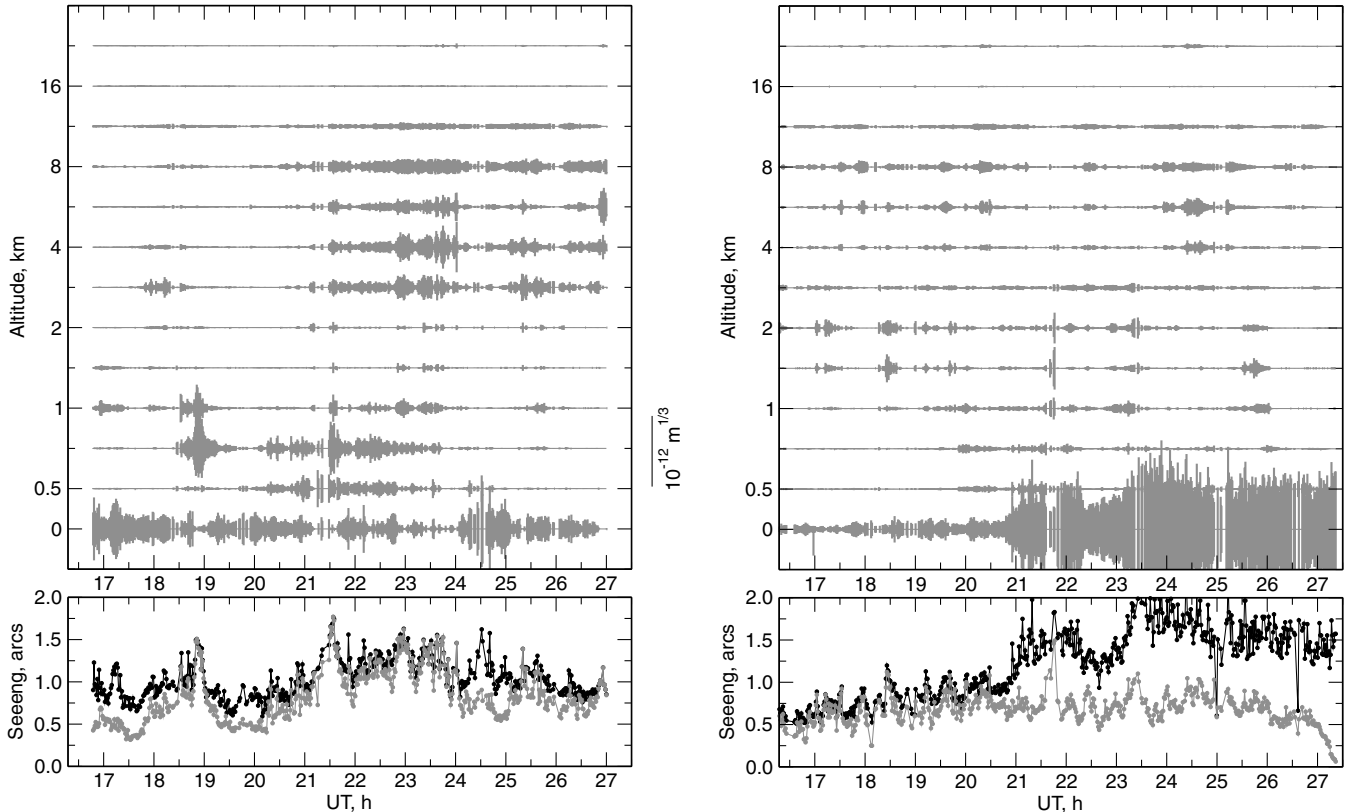


Figure 9. Examples of nightly data processing for 2009 February 19 (left) and 2009 October 24 (right). For each layer, the vertical bar length is proportional to the restored intensity. The scale is shown between the plots. Lower panels: records of seeing β_0 (whole atmosphere, black points) and free-atmosphere seeing β_{free} (grey points).

results for two nights that show different OT characters: on 2009 February 19 the conditions became worse after midnight when turbulence intensified at 3–8 km, and on 2009 October 24 a ground layer was responsible for the seeing deterioration. The wind data for this night report that at 22 h the ground wind became stronger and changed direction.

As previously said, the OT power can be characterized by different measures: intensity J , seeing β or Fried radius r_0 . The processing results are expressed in terms of J , but further on we will also use seeing, depending on the context. Quantities related to the whole atmosphere will be referred to as J_{total} and β_0 .

The discussion of OT at a given site and the subsequent use of results normally involves a distinction between ground and boundary layers. Here we consider layers at 0.5 km and above as ‘free atmosphere’. The respective turbulence intensity is denoted J_{free} .

A convenient and common way to present statistics of the OT vertical distribution is a cumulative distribution for the summed OT intensities from a given height h to the upper boundary of the atmosphere. In other words, these curves tell us the image quality for an observer at a given h . As shown in (Kornilov & Kornilov 2010), these integrals possess a higher precision than intensities in individual layers, since errors in adjacent layers anti-correlate.

Such cumulative distributions expressed in terms of seeing are shown in Fig. 10 (top). Their characteristic points are listed in Table 4. The graph at the bottom contains the most relevant distributions of β_0 and β_{free} . The distribution of β_0 derived from the OT profiles coincides with the one computed by the conventional DIMM formula to within ± 0.01 arcsec. For the free atmosphere, the difference between the OT profile and the integral moment-derived β_{free} is more visible but the median difference is only 0.04 arcsec.

The same plot shows the ‘winter’ (September–February) and ‘summer’ (March–August) seasonal distributions. Since the winter data are 2.4 times more voluminous, the ‘winter’ curve tends to fit the global one, differing by only 0.02 arcsec. The ‘summer’ seeing has a median of 1.00 arcsec.

Differential β_0 and β_{free} distributions allow us to determine the *mode* that characterizes the most probable value of seeing at Shatdzhatmaz. Since the curves are positively asymmetric, the modes are considerably less than the medians and equal to 0.82 and 0.35 arcsec, respectively.

It should be stressed that integral distributions, as well as the dependence of mean or median-layer intensity on its altitude, are useful for general statistical OT evaluation at a given site. However, they could scarcely help understanding of atmospheric processes since they do not reflect the correlations between turbulent layers.

Of considerable interest are the seasonal variations of characteristic OT quantities. Although we cover only two years of observations at Shatdzhatmaz and the monthly behaviour is not well defined, we may already conclude confidently from Table 5 that October and November deliver the best conditions in terms of both total turbulence and the free atmosphere. On the other hand, the end of winter (March) shows remarkably strong turbulence.

8.2 Ground-layer properties

Particularly important is the behaviour and characteristics of the ground layer as a dominant contributor to the turbulent atmosphere. In principle, simultaneous MASS and DIMM measurements allow us to extract its power as a difference of J_{total} and J_{free} values, which in fact originate from different instruments and methods. It is evident that systematic errors in their determination will amplify in the difference $J_{\text{total}} - J_{\text{free}}$. In cases in which the ground layer

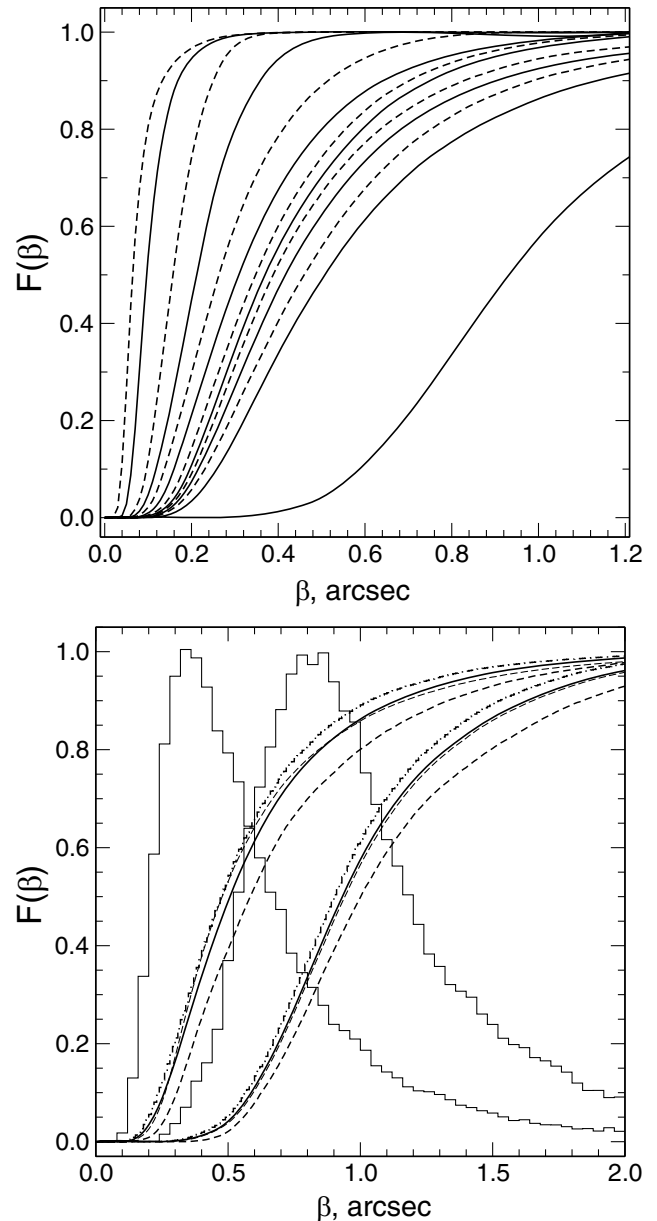


Figure 10. Top: integral distributions of the total OT intensity expressed as seeing β_h computed for atmosphere layers at h and above. Solid lines from right to left: total atmosphere, 0.5 km and higher, 1 km and higher, etc. for 2-, 4-, 8- and 16-km levels. Dashed lines are the same for intermediate heights. Bottom: integral distributions of the total image quality β_0 (right solid line) for the total data set, for winter (dash-dotted) and summer (dashed) seasons. The thin-dashed curve shows the distribution of β_0 computed using the conventional formula. The leftmost solid and thin curves present β_{free} derived from OT profiles and from the zero-order moment (integral atmosphere parameter M_0). The thin step-like curves are differential β_0 and β_{free} distributions.

dominates this is not very critical, but when it is weak or when the high-altitude turbulence is strong problems could arise.

Potential systematic biases of DIMM results have already been described and taken into account in the data processing. Meanwhile, the uncertainty noted in the slope type that is sensed by the DIMM instrument in particular has not been still experimentally examined. It is probably neither z -tilt nor g -tilt but some intermediate

Table 4. Quartiles of the OT intensity J (Q2 is the median) generated by the given altitude layer (in km) and the layers above and of the respective seeing β .

Layer	β (arcsec)			$J(\times 10^{-14} \text{ m}^{1/3})$		
	Q1	Q2	Q3	Q1	Q2	Q3
Whole	0.731	0.932	1.222	40.3	60.4	94.8
0.5+	0.349	0.508	0.760	11.8	21.9	43.0
0.71+	0.315	0.460	0.680	9.89	18.6	35.7
1.0+	0.291	0.417	0.617	8.68	17.0	30.4
1.41+	0.273	0.388	0.575	7.82	15.8	27.0
2.0+	0.261	0.370	0.542	7.23	14.0	24.5
2.82+	0.243	0.348	0.507	6.41	12.9	21.8
4.0+	0.214	0.309	0.455	5.20	9.58	18.2
5.66+	0.186	0.263	0.375	4.12	7.33	13.3
8.0+	0.157	0.212	0.279	3.10	5.10	8.10
11.3+	0.121	0.157	0.202	2.02	3.11	4.72
16+	0.076	0.097	0.128	0.92	1.38	2.19
22.6	0.049	0.064	0.090	0.45	0.70	1.22

Table 5. Monthly seeing distributions for the whole atmosphere and for layers at 1 km and above (in arcsec). N is the number of measurements in a given month.

Month	N (10^3)	Total seeing β_0			Free seeing β_1		
		Q1	Q2	Q3	Q1	Q2	Q3
Jan	5.0	0.77	0.98	1.28	0.27	0.42	0.63
Feb	7.8	0.82	1.00	1.28	0.37	0.56	0.87
Mar	3.9	1.30	1.70	2.06	0.55	0.88	1.35
Apr	4.7	0.75	1.02	1.45	0.28	0.39	0.58
May	2.9	0.73	0.95	1.38	0.30	0.39	0.60
Jun	4.3	0.78	0.91	1.10	0.35	0.43	0.54
Jul	3.6	0.80	0.93	1.12	0.38	0.53	0.71
Aug	5.6	0.70	0.95	1.16	0.31	0.46	0.65
Sep	5.3	0.80	0.97	1.21	0.29	0.38	0.55
Oct	18.5	0.64	0.82	1.04	0.23	0.34	0.50
Nov	11.0	0.65	0.84	1.16	0.26	0.36	0.52
Dec	13.0	0.78	0.97	1.25	0.32	0.44	0.61

characteristic. The maximum resulting uncertainty is about 17 per cent in intensity or 10 per cent in seeing.

There are biases in the MASS data processing as well, described in detail by Tokovinin & Kornilov (2007). The most significant is a deviation from the weak-perturbation approximation in the case of strong high turbulence, causing near-saturated scintillation to develop in small apertures. Although the above-mentioned authors do provide some empirical correction, the derived solution is formally worse by the R^2 criterion. That is why the `ATMOS-2.96` data processor makes only the following corrections of scintillation indices:

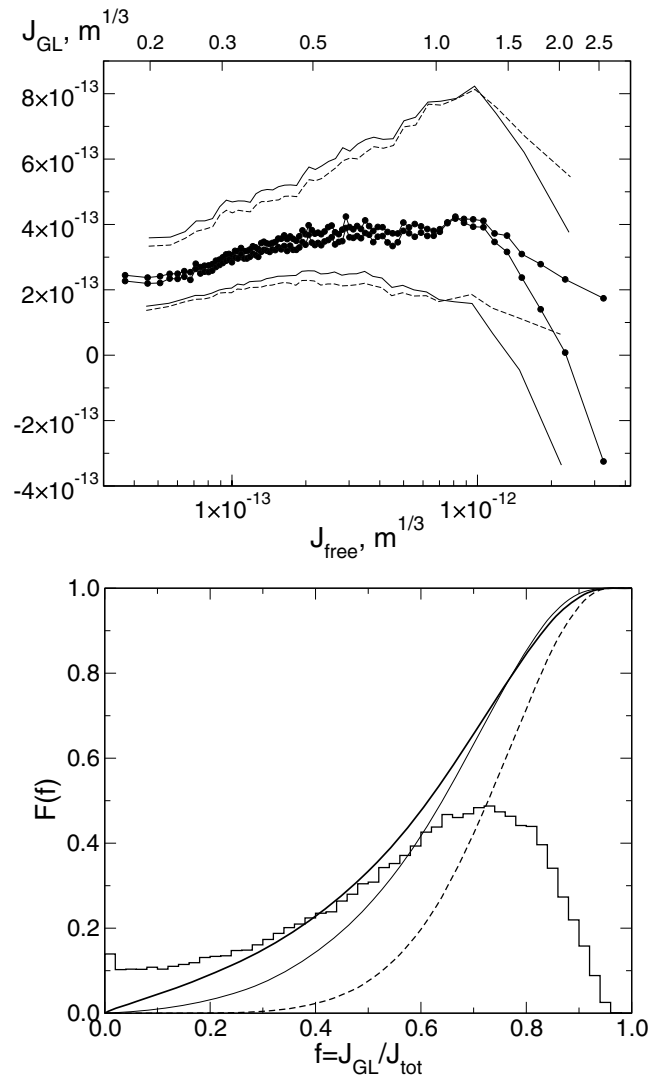
$$s^2 = \ln(\bar{s}^2 + 1), \quad (9)$$

where \bar{s}^2 is the computed index in a sense $\langle \delta I^2 \rangle / \langle I \rangle^2$. The reason is that the MASS weighting functions are defined for $\chi = \ln A$ fluctuations, where A is a light-wave amplitude and the scintillation index is defined as $s^2 = 4\sigma^2$, where σ^2 is a variance of χ . The measured light intensity has a log-normal distribution and for a strong scintillation ($s^2 \sim 0.5$) this leads to a 20 per cent error.

This problem was also discussed in the past, but consideration of nearly saturated scintillation has restrained us from additional diminishing of the scintillation indices. Nevertheless, examination of real data has shown that the described correction works in the right way: the OT power becomes weaker and the turbulence itself tends to localize at higher levels.

The first estimation of the ground-layer intensity \hat{J}_{GL} was obtained from the altitude turbulence moments and the conventional formula (5). Our study reveals that application of the correction (9) decreases the fraction of problematic data from ≈ 0.10 to < 0.04 , and such data do not originate from random errors in the ground-layer intensity determination.

In Fig. 11 we show the dependence of the median values \hat{J}_{GL} (calculated over groups of 1000 points) on J_{free} . It is clear that in conditions of a very weak (about $4 \times 10^{-14} \text{ m}^{1/3}$) free-atmosphere OT $\hat{J}_{\text{GL}} \approx 2 \times 10^{-13} \text{ m}^{1/3}$ (nearly 0.5 arcsec), i.e. it exceeds the J_{free} intensity significantly. As turbulence gets stronger, \hat{J}_{GL} increases. Such a relation indicates a weak and most probably indirect interrelation between the ground layer and the free atmosphere. Further, the ground-layer intensity stabilizes at the level $4 \times 10^{-13} \text{ m}^{1/3}$ (≈ 0.7 arcsec) and remains unchanged while $J_{\text{free}} < 1 \times 10^{-12} \text{ m}^{1/3}$ (≈ 1.3 arcsec).

**Figure 11.** Top: dependence of the median ground-layer power as obtained from integrals J_{total} and J_{free} (black dots) and from OT profiles (open circles) on the intensity J_{free} . Thin solid and dashed curves depict the first and third quartiles of the respective distributions. Bottom: integral distribution of the ground-layer intensity fraction for the total data set (thick solid line), the $\beta_0 < 0.93$ arcsec subset (thin solid) and the $\beta_{\text{free}} < 0.50$ arcsec subset (dashed). The stair curve is the differential total distribution.

The ground-layer intensity \check{J}_{GL} derived from the OT-profile restoration behaves in a similar way. Meanwhile, when the free-atmosphere turbulence becomes too strong and the above-mentioned systematic effects cause \hat{J}_{GL} to drop, tending to negative values, \check{J}_{GL} remains positive.

Such a difference is explained by propagation effects becoming significant for DIMM measurements in dominant free-atmosphere turbulence conditions. An additional circumstance is a non-negativity restriction applied in OT restoration, which acts similarly to saturated-index correction, i.e. decreasing and raising the resulting turbulence.

In Fig. 11 (bottom) we plot the differential and integral distributions of the fractional power f of the ground layer. The integral distribution of all measurements demonstrates the systematics in the small- f domain, with a small excess of zero values. This shows that the implemented correction is not sufficient, although it prevents negative \check{J}_{GL} values.

These effects are diminished in the f distribution for the cases of β_0 better than median and are absent in $\beta_{free} < 0.50$ arcsec conditions. Note that the distribution is highly asymmetric, due to the nature of f as a ratio, so the mode and the median are largely different. For the total data set, the mode and the median are 0.71 and 0.61, for the sample $\beta_0 < 0.93$ arcsec they are 0.71 and 0.64, and when $\beta_{free} < 0.50$ arcsec they are 0.78 and 0.73.

One might expect that complete correction for saturation would make the total data distribution closer to the good-image case, i.e. the median fraction of the ground layer would increase to ≈ 0.65 . This value is typical for many summits (at Las Campanas observatory $f = 0.63$, as Thomas-Osip et al. (2008) quote) except for those good sites that have a very thin ground layer, e.g. $f = 0.46$ at Mauna Kea (Skidmore et al. 2009).

8.3 Structure of the turbulent atmosphere

Many authors (e.g. see Tokovinin & Travouillon 2006) note that the OT distribution character depends on the total intensity. In order to study the properties of the OT structure on the basis of the restored profiles, the median-layer intensity fractions were plotted in Fig. 12 for the whole atmosphere and for the free one. Note that in these pictures a layer fraction is the *width* of the respective stripe.

In the top graph the full-atmosphere structure is plotted against J_{total} . The abrupt lowering of the ground-layer fraction above $J_{total} = 1 \times 10^{-12} \text{ m}^{1/3}$ is related to systematic effects in its determination, as discussed in the previous section. In the weaker turbulence domain a real diminishing of its fraction from 0.7 to 0.6 is seen. The summed intensity of the ground and 0.5-km layers accounts for about 0.70 of the total power in the whole J_{total} range.

It is informative that strengthening of the total turbulence is powered by the growth of lower 0.5 and 0.7 km layers which belong to the boundary region of the atmosphere and also by the 4 and 6 km layers. This is accompanied by diminishing the 8–16 km layer contribution, which normally dominates when the total OT is weak. The increasing role of the lower layers may be ascribed to the thickening of the ground layer in bad conditions.

Changes in the free-atmosphere structure as they evolve with its overall power are shown in the bottom plot of Fig. 12. The general tendency is an increase in the fraction of low layers with increasing total intensity of the OT in the free atmosphere. The whole range can be subdivided into three domains: $\beta_{free} < 0.3$ arcsec, $\beta_{free} > 1.0$ arcsec and an intermediate. The leftmost region, corresponding to the best conditions, shows the layers above 8 km dominating;

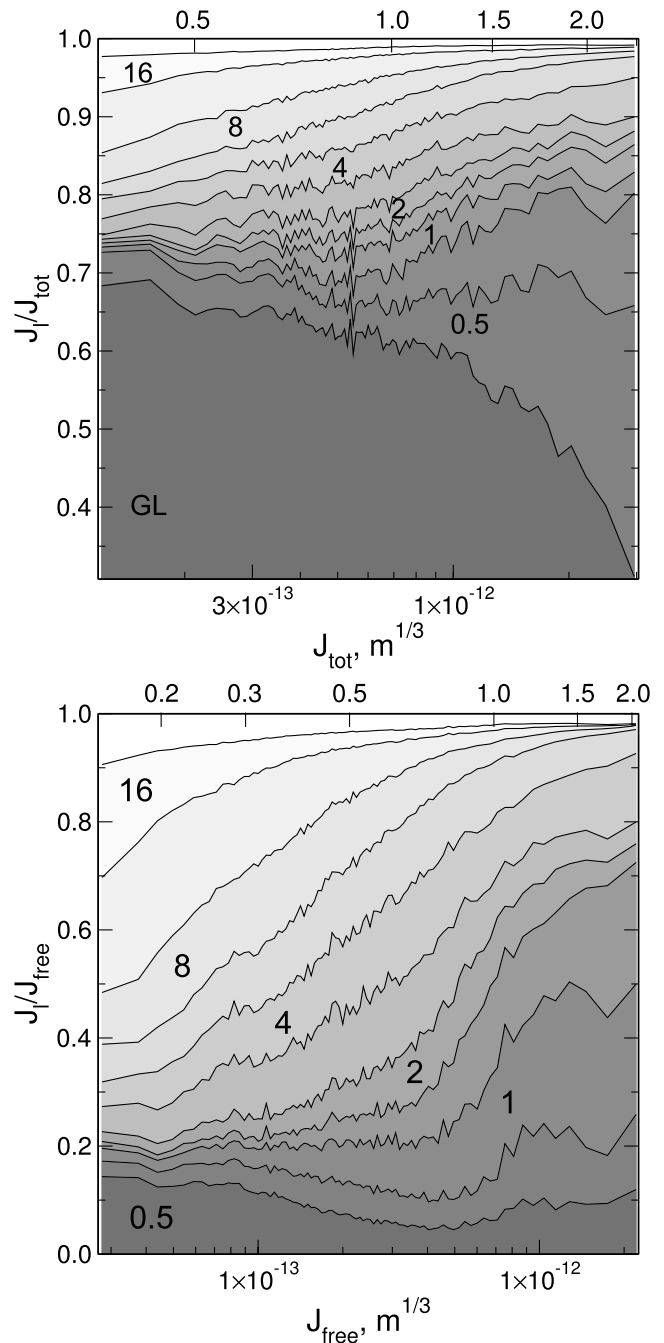


Figure 12. Structure of the turbulent atmosphere as a function of total intensity J . The stripe thickness reflects its fraction of the total. Top: the whole atmosphere structure as a function of J_{total} (i.e. including GL). Bottom: the free-atmosphere structure as a function of J_{free} . Alternative (upper) x-axes provide the seeing scale in arcsec.

in intermediate conditions the major OT contribution descends to 2–8 km, and in the worst situation down to 0.7–1.4 km.

8.4 Integral parameters

In addition to the OT-profile restoration, the computed scintillation indices also serve for calculation of the altitude moments of turbulence as described in TKSv:

$$M_\alpha = \int C_n^2(h) h^\alpha dh, \quad (10)$$

for $\alpha = 0, 1, 5/3, 2$. These moments are used for integral atmospheric-parameter determination: free-atmosphere seeing $\beta_{\text{free}}^{5/3} \sim M_0$, effective OT altitude $h_{\text{eff}} \sim M_1$, isoplanatic angle $\theta_0^{-5/3} \sim M_{5/3}$ and isokinetic angle $\theta_k^{-2} \sim M_2$. From the s_A^2 scintillation indices obtained with a tripled exposure, the atmospheric coherence time τ_0 is estimated as proposed by Tokovinin (2002b). In these terms, the seeing β_0 obtained by formula (5) is also a kind of integral parameter.

Atmospheric moments are computed as linear scintillation-index combinations where the related coefficients are derived from the required h^α approximations using the weighting functions $Q(h)$ (TKSV). A feasible precision ($\delta < 0.05$) of this decomposition is attained at altitudes $h > 0.4$ km, which is sufficient because lower layers produce almost no scintillation.

The isoplanatic angle determined from $M_{5/3}$ agrees well with the angles computed from OT profiles. The regression slope is 0.98 with a root-mean-square scatter of 0.03 arcsec around it. The median θ_0 from profiles is 2.03 arcsec, differing by less than 2 per cent from the θ_0 median calculated from the moments. This fact adds confidence to the results of OT restoration using the implemented algorithm.

Integral θ_0 distributions for three samples (the full scope of the data and the cases $\beta_0 < 0.93$ arcsec and $\beta_0 < 0.73$ arcsec) are shown in Fig. 13 (left) and their characteristics are listed in Table 6. Since θ_0 is essentially driven by turbulence in the upper atmosphere, its value is tied to the altitude of the summit. Given this circumstance, the value obtained is as good as at many other observatories.

For example, our MASS measurements at Maidanak (Kornilov et al. 2009) derived a characteristic θ_0 of 2.19 arcsec, varying seasonally from 1.92–2.35 arcsec. Els et al. (2009) and Tokovinin & Travouillon (2006) list $\theta_0 = 1.56$ and 2.22 arcsec for Cerro Tololo and Cerro Pachon, respectively.

Values of the AO time constant τ_0 delivered by MASS and listed in Table 7 do not correspond to the standard definition of this quantity,

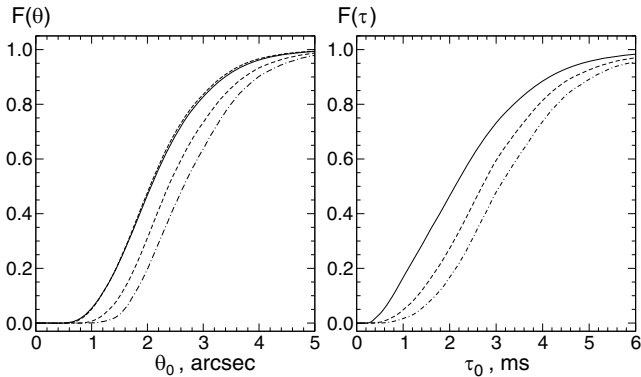


Figure 13. Left: integral isoplanatic angle θ_0 distributions for the whole data set (solid line), $\beta_0 <$ median subset (dashed) and $\beta_0 <$ 25 per cent (dash-dotted). The leftmost dashed line depicts θ_0 from OT profiles. Right: integral distributions of atmospheric constant τ_0 for the same data samples.

Table 6. Cumulative statistics of integral atmospheric parameters. Isoplanatic and isokinetic angles θ_0 and θ_k are in arcsec.

	θ_0			θ_k		
	Q1	Q2	Q3	Q1	Q2	Q3
Whole set	1.56	2.07	2.70	5.54	7.00	8.67
Best 50 per cent of β_0	1.88	2.38	3.06	6.42	7.78	9.52
Best 25 per cent of β_0	2.11	2.65	3.33	7.04	8.46	10.17

Table 7. Cumulative statistics of the time constant τ_0 , in ms.

	τ_0			τ_0 correct.		
	Q1	Q2	Q3	Q1	Q2	Q3
Whole set	1.28	2.12	3.09	1.59	2.58	3.70
Best 50 per cent of β_0	1.92	2.70	3.67	2.40	3.34	4.46
Best 25 per cent of β_0	2.32	3.08	4.06	–	–	–

as noted by many authors. The estimates obtained by this method require a certain correction (see, for example, Travouillon et al. 2009). For correction of individual values, we used formula (3) from the updated study of A. Tokovinin.¹³ The statistics for the corrected τ_0 are also shown in Table 7.

Isokinetic angle θ_k , which provides the angular size of the wavefront-slope correlation, has a special property that depends not only on the wavelength but also on the telescope aperture. According to Hardy (1998), it is related to the turbulence second moment by the following expression:

$$\theta_k^{-2} = 0.688 \left(\frac{2\pi}{\lambda} \right)^2 D^{-1/3} M_2. \quad (11)$$

In Table 6 the characteristics of the observed θ_k distribution are given for the case of $\lambda = 500$ nm and telescope $D = 2.5$ m. Comparison with the value derived from OT profiles shows very good coincidence; the median isokinetic angle equals 7.01 arcsec. Explicit measurement of θ_k is omitted in the majority of site-testing campaigns since it strongly correlates with the isoplanatic angle and depends (although weakly) on the aperture size.

9 DISCUSSION AND CONCLUSIONS

9.1 Discussion of results

Detailed analysis and interpretation of the results obtained extends beyond the framework of the current study. Here we limit ourselves to two examples of potential uses of the information provided.

Various statistics of seeing and other relevant parameters are not sufficient for comprehensive characterization of the turbulent atmosphere properties at a given site. The temporal characteristics describing the typical rate of OT evolution, its time-scales of stability, and so on are of great importance. These issues will be examined in forthcoming papers. In the current study we provide only a crude estimate of the temporal stability of seeing in a form suitable for a typical astronomical application.

In Fig. 14 we show the fractions of observing time suitable to deliver continuous periods E of seeing better than a selected threshold. For example, 30-min exposures with an image quality better than 0.6 arcsec are possible for 3 per cent of the available observing time, which corresponds to 80 such exposures per year. If we restrict ourselves to 15-min exposures, we will obtain more than 230 frames per year. Such a statistic is evidently over-constrained, since short-term image deteriorations do not spoil the images that seriously, but these ‘almost good’ exposures would not be counted. A similar prognosis of OT stability was presented in the paper of Travouillon et al. (2008).

Turbulence generation in the ground layer is usually related to mixing of local air masses by the wind. A characteristic feature of this phenomenon is the dependence of turbulence intensity on the

¹³ <http://www.ctio.noao.edu/atokovin/profiler/timeconstnew.pdf>

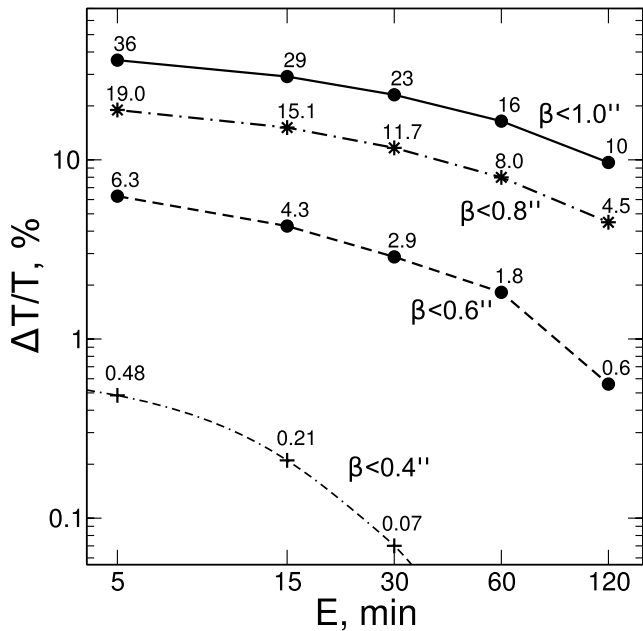


Figure 14. Fraction of available continuous astronomical exposures of duration E with a given limit of seeing β_0 .

ground wind speed. Such a correlation is observed at many sites, as reported by Thomas-Osip et al. (2008) and Skidmore et al. (2009). In Fig. 15 we plot the median seeing for the ground layer, free and full atmosphere as a function of the recorded ground wind speed. These medians were calculated over groups of 1000 points. The effect is quite prominent, as reflected by the median-value spread and interquartile range shown for β_0 .

It is also evident from the β_{GL} curve that strengthening of the ground wind first causes a decrease of the detected seeing, which reaches a minimum at speeds $1.5\text{--}2\text{ m s}^{-1}$ and then starts getting worse for speeds up to 4 m s^{-1} . A similar effect is noted by

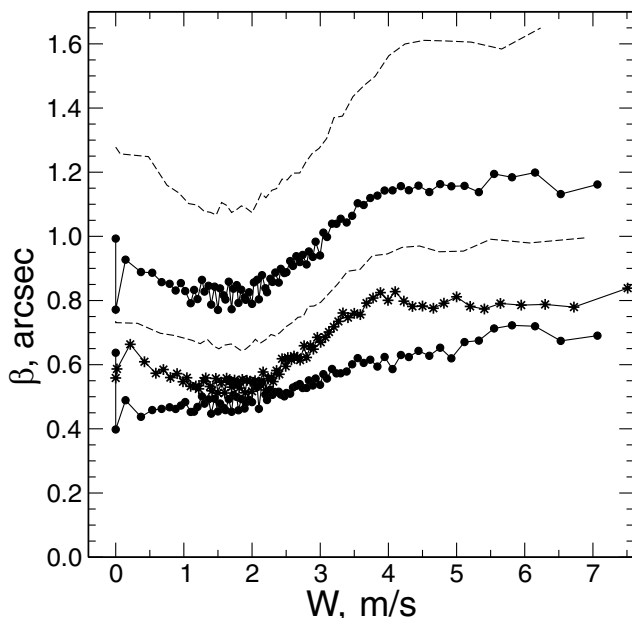


Figure 15. Dependence of the median seeing β_0 (black dots), β_{free} (open circles) and β_{GL} (stars) on the ground wind speed W . Dashed lines depict the first and third quartiles for β_0 .

Skidmore et al. (2009) at all monitored sites except San Pedro Martir. Further wind-speed growth has no effect on the ground turbulence but apparently increases the boundary-layer seeing at 0.5 km and higher. It is remarkable that the minimum β_{GL} corresponds to the most probable wind speed at Shatdzhatmaz in clear night conditions, 2 m s^{-1} .

9.2 Conclusions

The measured basic site characteristics and OT profiles have confirmed the efficiency of the developed and built automatic site monitor. The OT data amount and quality exceed very significantly the results of our previous three-year campaign performed at Mt Maidanak in 2005–2007 in the manual-observation mode (Kornilov et al. 2009). This convincingly justifies the time and resources invested in the complete automation of astronomical monitoring measurements.

Here we list the most significant site characteristics determined in the site-testing program at Mt Shatdzhatmaz in 2007–2009.

- (i) The annual clear astronomical night-time is 1343 h and the clear nautical night-time is 1546 h, under a rather strict clear-sky criterion.
- (ii) The maximum of the clear-sky amount is observed from mid-September to mid-March, where about 70 per cent of the clear weather is concentrated.
- (iii) The mean clear night-time temperature is $+1.8^\circ\text{C}$, which implies a moderate water-vapour content in the atmosphere.
- (iv) On clear nights, the median precipitable water vapour is 7.75 mm.
- (v) The day-to-night temperature contrast is $\approx 3.4^\circ\text{C}$ for clear-sky weather.
- (vi) The median ground wind speed is 2.3 m s^{-1} with a preferred direction from the west.
- (vii) The median seeing β_0 is 0.93 arcsec. For 25 per cent of the time $\beta_0 < 0.73$ arcsec. The most probable seeing value is 0.82 arcsec.
- (viii) The free-atmosphere median seeing β_{free} is 0.51 arcsec; the mode is 0.35 arcsec.
- (ix) The best seeing (minimal OT strength) is observed in October–November. The typical median value for that period is ≈ 0.83 arcsec.
- (x) In conditions of seeing better than the median value the optical turbulence is dominated by the ground layer: its fraction reaches 0.65.
- (xi) Periods of bad image quality occur when OT in the boundary and free atmosphere intensifies.
- (xii) The median isoplanatic angle is 2.07 arcsec in general and 2.38 arcsec in conditions of seeing better than the median.
- (xiii) The median-corrected atmospheric time constant is 2.58 ms; it exceeds 3.3 ms in conditions of weak turbulence.

These results are based on only two years of monitoring and reflect the current situation at the site under evaluation. It is well known that astroclimate parameters are subject to long-term trends and cycles, so continued monitoring may introduce certain corrections. That is why we will proceed further with the ASM operation. When the 2.5-m telescope is put into operation at the observatory, the ASM functionality will be involved in flexible observation planning.

A more extended site astronomical characterization demands the monitoring of atmospheric extinction (also in the infrared domain),

sky-background level and characteristics important for AO such as the altitude wind-speed profile.

Nevertheless, it is already possible to characterize the potential of the summit studied as moderately high for astronomical observations. The basic parameters are slightly worse with respect to those of leading astronomical observatories, but not very significantly. Our main conclusion is that modern methods of improving telescope resolution will prove efficient at Shatdzhatmaz.

ACKNOWLEDGMENTS

The reported site testing and OT-property research at Mt Shatdzhatmaz were performed under the partial support of the RFBR (grant 06-02-16902). The authors are grateful to the Pulkovo Solar Station staff, Sternberg Institute colleagues P. Kortunov, A. Belinsky, M. Kuznetsov and E. Gorbovskoy and students of the astronomical department of the Moscow University physical faculty for their help in the work. Special thanks is due to A. Tokovinin for much advice and numerous discussions on the OT research problems throughout the project.

REFERENCES

- Avila R., Avilés J. L., Wilson R. W., Chun M., Butterley T., Carrasco E., 2008, *MNRAS*, 387, 1511
- Boshnjakovitch N. A., Bystrova N. V., Demidova A. N., Zhukova L. N., Kassinsky V. V., Eerme K. A., 1962, *Izvestiia GAO v Pulkove*, 22, 155
- Bowen I. S., 1964, *AJ*, 69, 816
- Carrasco E., Avila R., Carramiñana A., 2005, *PASP*, 117, 104
- Darchiya A. H., Schmeel L. F., Darchiya S. P., 1960, *Izvestiia GAO v Pulkove*, 21, 52
- Depenchuk E. A., Kondratyuk R. R., Kojfman A. P., 1977, *Astrometrija i Astrofizika. Vyp. (No.) 31. Naukova dumka, Kiev*, p. 99
- Ehgamberdiev S. A., Baijumanov A. K., Ilyasov S. P., Sarazin M., Tillayev Y. A., Tokovinin A. A., Ziad A., 2000, *A&AS*, 145, 293
- Els S. G. et al., 2009, *PASP*, 121, 922
- Fuchs A., Tallon M., Vernin J., 1998, *PASP*, 110, 86
- Fuensalida J. et al., 2004, in Ardeberg A. L., Andersen T., eds, *Proc. SPIE Vol. 5382, Second Backaskog Workshop on Extremely Large Telescopes*. SPIE, Bellingham, p. 619
- Gnevysheva K. G., 1991, *Izvestiia GAO v Pulkove*, 207, 77
- Hardy J. W., 1998, *Adaptive Optics for Astronomical Telescopes*. Oxford Univ. Press, Oxford
- Kornilov V., Kornilov M., 2010, preprint (arXiv:1005.4658)
- Kornilov V., Tokovinin A., Voziakova O., Zaitsev A., Shatsky N., Potanin S., Sarazin M., 2003, in Wizinovich P. L., Bonaccini D., eds, *Proc. SPIE Vol. 4839, Adaptive Optical System Technologies II*. SPIE, Bellingham, p. 837
- Kornilov V., Tokovinin A., Shatsky N., Voziakova O., Potanin S., Safonov B., 2007, *MNRAS*, 382, 1268
- Kornilov V., Ilyasov S., Vozyakova O., Tillaev Yu., Safonov B., Ibragimov M., Shatsky N., Egamberdiev Sh., 2009, *Astron. Lett.*, 35, 547
- Leushin V. V., Nelyubin N. F., Nebelitskij V. B., Novikov S. B., 1975, *Astron. Tsirk*, 866, 6
- Lipunov V. et al., 2010, *Adv. Astron.*, 2010, 1
- Martin H. M., 1987, *PASP*, 99, 1360
- Nelyubin N. F., Vasilyev O. B., 1969, *Astrofiz. Issled. Izv. Spets. Astrofiz. Obs.*, 1, 185
- Riddle R., Schoeck M., Skidmore W., 2006, in Stepp L., ed., *Proc. SPIE Vol. 6267, Ground-based and Airborne Telescopes*. SPIE, Bellingham, p. 62671Q
- Roddier F., 1981, in Wolf E., ed., *Progress in Optics*, 19. North-Holland, Amsterdam, p. 281
- Roddier F., 1999, *Adaptive Optics in Astronomy*. Cambridge Univ. Press, Cambridge
- Rylkov V. P., Bobylev V. V., 1991, *Izvestiia GAO v Pulkove*, 207, 89
- Sarazin M., Roddier F., 1990, *A&A*, 227, 294
- Saunders W. et al., 2009, *PASP*, 121, 976
- Schoeck M. et al., 2009, *PASP*, 121, 384
- Skidmore W., Els S., Travouillon T., Riddle R., Schöck M., Bustos E., Seguel J., Walker D., 2009, *PASP*, 121, 1151
- Soules D. B., Drexler J. J., Draayer B. F., Eaton F. D., Hines J. R., 1996, *PASP*, 108, 817
- Tatarskii V. I., 1967, *Wave Propagation in a Turbulent Medium*. Dover Press, New York
- Thomas-Osip J. E., Prieto G., Johns M., Phillips M. M., 2008, in Stepp L. M., Gilmozzi R., eds, *Proc. SPIE Vol. 7012, Ground-based and Airborne Telescopes II*. SPIE, Bellingham, p. 70121U
- Thomsen M., Britton M., Pickles A., 2007, *BAAS*, 38, 242
- Tokovinin A., 2002a, *PASP*, 114, 1156
- Tokovinin A., 2002b, *Appl. Optics*, 41, 957
- Tokovinin A., Kornilov V., 2007, *MNRAS*, 381, 1179
- Tokovinin A., Travouillon T., 2006, *MNRAS*, 365, 1235
- Tokovinin A., Baumont S., Vasquez J., 2003a, *MNRAS*, 340, 52
- Tokovinin A., Kornilov V., Shatsky N., Voziakova O., 2003b, *MNRAS*, 343, 891 (TKSV)
- Tokovinin A., Sarazin M., Smette A., 2007, *MNRAS*, 378, 701
- Tokovinin A., Bustos E., Berdja A., 2010, *MNRAS*, 404, 1186
- Travouillon T. et al., 2008, in Stepp L. M., Gilmozzi R., eds, *Proc. SPIE Vol. 7012, Ground-based and Airborne Telescopes II*. SPIE, Bellingham, p. 701220
- Travouillon T., Els S., Riddle R. L., Schöck M., Skidmore W., 2009, *PASP*, 121, 787
- Vernin J., Caccia J.-L., Weigelt G., Mueller M., 1991, *A&A*, 243, 553
- Vernin J., Muñoz-Tuñón C., Sarazin M., 2008, in Stepp L., Gilmozzi R., eds, *Proc. SPIE Vol. 7012, Ground-based and Airborne Telescopes II*, p. 70121T
- Wilson R. W., 2002, *MNRAS*, 337, 103
- Wilson R. W., Wooder N. J., Rigal F., Dainty J. C., 2003, *MNRAS*, 339, 491
- Wilson R., Butterley T., Sarazin M., 2009, *MNRAS*, 399, 2129

This paper has been typeset from a $\text{\TeX}/\text{\LaTeX}$ file prepared by the author.